

Structuration of the Surface Layer during Drying of Colloidal Dispersions

Marguerite Léang,^{†,‡} Didier Lairez,^{†,§} Fabrice Cousin,[†] Frédérique Giorgiutti-Dauphiné,[‡] Ludovic Pauchard,[‡] and Lay-Theng Lee^{*,†}

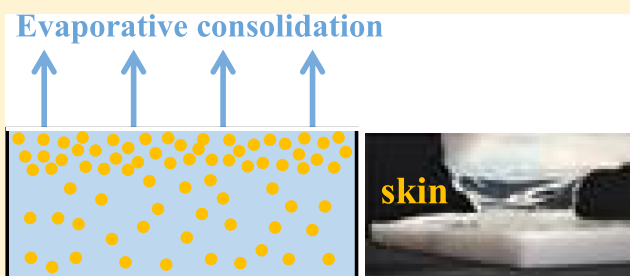
[†]Laboratoire Léon Brillouin, CEA-CNRS, Université Paris-Saclay, CEA-Saclay, 91191 Gif sur Yvette Cedex, France

[‡]Laboratoire F.A.S.T., Université Paris-Sud, CNRS, Université Paris-Saclay, F-91405 Orsay, France

[§]Laboratoire des Solides Irradiés, Ecole Polytechnique, CEA-CNRS, Université Paris-Saclay, 91128 Palaiseau Cedex, France

Supporting Information

ABSTRACT: During evaporative drying of a colloidal dispersion, the structural behavior at the air–dispersion interface is of particular relevance to the understanding of the consolidation mechanism and the final structural and mechanical properties of the porous media. The drying interface constitutes the region of initial drying stress that, when accumulated over a critical thickness, leads to crack formation. This work presents an experimental study of top-down drying of colloidal silica dispersions with three different sizes (radius 5, 8, and 13 nm). Using specular neutron reflectivity, we focus on the structural evolution at the free drying front of the dispersion with a macroscopic drying surface and demonstrate the existence of a thick concentrated surface layer induced by heterogeneous evaporation. The reflectivity profile contains a strong structure peak due to scattering from particles in the interfacial region, from which the interparticle distance is deduced. A notable advantage of these measurements is the direct extraction of the corresponding dispersion concentration from the critical total reflection edge, providing a straightforward access to a structure–concentration relation during the drying process. The bulk reservoir of this experimental configuration renders it possible to verify the evaporation–diffusion balance to construct the surface layer and also to check reversibility of particle ordering. We follow the structural evolution of this surface layer from a sol to a soft wet-gel that is the precursor of a fragile skin and the onset of significant particle aggregation that precedes formation of the wet-crust. Separate complementary measurements on the structural evolution in the bulk dispersion are also carried out by small-angle neutron scattering, where the particle concentration is also extracted directly from the experimental curves. The two sets of data reveal similar structural evolution with concentration at the interface and in the bulk and an increase in the degree of ordering with the particle size.



INTRODUCTION

Drying of colloidal dispersions is a common phenomenon encountered in daily experiences such as in beverage stains¹ and in technological applications where numerous examples can be found in review papers:^{2–4} coatings, ink jet printing, magnetic tape casting, optical devices, and agricultural sprays; other examples refer to paint layers in art and cultural heritage objects.^{5–7} Drying can be edge-in or top-down and involves consolidation, compaction, solidification, and crack formation for films above a critical thickness sufficient to store and release elastic energy.^{8–10} The final film properties depend on a complex interplay of the physico-chemical parameters of the dispersion^{11–14} and the substrate^{10,15,16} as well as the drying conditions.^{17,18} Therefore, considerable interest has been vested in understanding and controlling the final properties and morphologies of drying colloidal films. Past studies have reported on thin films,^{19,20} especially in confined geometry^{21–27} and on droplets,^{11,12,28,29} and to avoid substrate effects, studies of microdroplets suspended from a capillary

have also been reported.³⁰ Much interest has also focused on crack formation and propagation^{31–33} and on parameters that control the final microstructures such as particle size¹³ and interactions.^{11,12,14} The cracks that are formed vary in morphology and also in length scale, from micron-scale as in paintings^{6,7} to geological-scale as in soil and mud cracks.³⁴

An interesting aspect in free-drying films is the non-homogeneous drying profile that leads to the formation of a crust.^{35,36} Depending on the rate of liquid evaporation that concentrates the particles and the diffusion of particles back into the bulk, a crust of consolidated particles is predicted to form on top of the fluid dispersion. This crust, similar to the skin that is formed by aggregated soft latex particles in drying paints and aggregated protein skin on boiled milk, is more easily observable for thick films than for very thin films that dry

Received: November 8, 2018

Revised: December 20, 2018

Published: February 5, 2019

quickly and linearly. Thus, in very thin films and small droplets, the presence of a skin is often an indirect attribute to explain surface mechanical instability that causes buckling and invagination that generate fascinating morphologies of the drying drops.^{37–39}

Crust formation therefore is an important phenomenon in the drying of colloidal dispersions. In spite of this practical implication, relatively little work exists on the study of the crust layer. In this paper, we present an experimental study of the structural evolution up to the regime of wet-crust formation in drying macroscopic volume of colloidal silica dispersions. The drying process is top-down where particle organization and structural evolution at the drying front are investigated using neutron reflectivity and scattering. These surface measurements are carried out away from edge effects and pinning lines. This geometry can thus be considered as a laterally homogeneous suspended film with a drying front at the dispersion–air interface and a wet-front in contact with the bulk dispersion reservoir. The sample surface area probed is several cm² and measurements are carried out over a timescale of hours covering structural evolution from dilute dispersions up to the onset of crust formation. This wet-crust region is of special importance in the context of stress development and crack formation and the related mechanical properties of the final porous media. To our knowledge, there has not been any experimental report on the structural properties of this crust region under the current drying geometry. Our work here focuses on structural evolution leading to this critical region: sol–gel transition, aggregation, reversibility, and macroscopic wet-crust formation. Complementary measurements of the bulk volume structure are also carried out using small-angle neutron scattering (SANS).

MATERIALS AND EXPERIMENTAL METHODS

Three silica colloidal dispersions were used: Ludox SM30, HS40, and TM50 from Sigma-Aldrich with initial mass fractions of about 0.3, 0.4, and 0.5, respectively. The dispersions stabilized at pH between 9 and 10 were used as received. The particle radius a and the log-normal polydispersity σ/a characterized by SANS are SM30: $a = 4.7$ nm, $\sigma/a = 0.20$; HS40: $a = 7.9$ nm, $\sigma/a = 0.16$; TM50: $a = 12.8$ nm, $\sigma/a = 0.14$.

Measurements of structural properties at the interface were carried out using specular neutron reflectivity on the time-of-flight neutron reflectometer HERMES at the ORPHEE reactor (Laboratoire Léon Brillouin, CEA-Saclay). The liquid sample container was a Teflon trough (35 × 95 mm) positioned on an aluminum cell with a hermetic cover with quartz windows to allow the neutron beam to pass through with minimal absorption; the entire setup was placed on an antivibration support. The neutron beam wavelength range was $\lambda = 2$ –28 Å, and the grazing incident angle used was $\theta = 0.66^\circ$, giving a corresponding wave vector range, $Q = 0.005$ – 0.07 Å⁻¹. Under this configuration, there was adequate total reflection plateau. This plateau was useful for the normalization of the reflectivity curves, but more importantly the total reflection edge, Q_c , is a function of the sample scattering length density and thus of the composition of the dispersion.

For these experiments, an initial dispersion volume of 12.5 mL was deposited in the Teflon cell, giving a total sample thickness of about 3.7 mm. The liquid sample formed a large convex surface that allowed the reflectivity measurement to be performed on the free surface (about 93 mm × 36 mm), away from edge and line pinning zones of the liquid with the container. Under the current configuration, the vertical depth probed is of the order of a few hundred microns. For dispersions under equilibrium condition (no evaporation), measurements were performed with the sample enclosed hermetically with the cell cover. For drying samples, the cell cover was removed and in situ

measurements were carried out as the sample underwent evaporative drying under ambient conditions at temperature $T \approx 23$ °C and relative humidity (RH) ≈ 30 – 40% (see Figure 1). The reflectivity

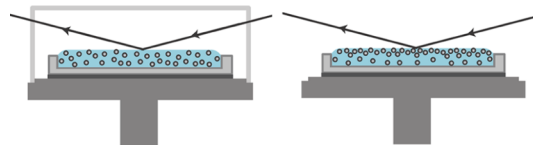


Figure 1. Schematic of the setup for neutron reflectivity measurement of a silica dispersion. The liquid sample is contained in a Teflon cell positioned on a hermetically closed aluminum cell with quartz windows; the ensemble is placed on an antivibration table. Left: equilibrium measurements with the hermetic cover; right: drying measurements without the cover.

spectra were acquired between 20 min and 1 h intervals depending on the initial dispersion concentration. Before each acquisition, a vertical scan of the sample height, z , was performed to align the liquid surface. Such z -scans (accuracy of the order of 20 μm) also allowed us to follow the decrease in liquid height as a function of the evaporation time.

For bulk measurements, SANS experiments were carried out on the PACE spectrometer at the ORPHEE reactor. For dilute dispersions, a classic 1 mm Hellma quartz cell was used. For the drying dispersions, the samples were dried horizontally on a circular cell with a final thickness of 1 mm. Four configurations were used, with sample detector distance from 1 to 5 m and wavelength from 6 to 17 Å, covering a total Q -range between 0.0024 and 0.37 Å⁻¹.

BASICS OF DRYING PROCESS

During drying of a dispersion, solvent evaporation concentrates particles near the surface. In the absence of convection, the only mass transfer with the underlying bulk liquid is diffusion that can be treated in one dimension if the surface is sufficiently large. At the beginning of the process, this interplay between evaporation and diffusion governs the variation with time of the particle concentration profile. We denote here ϕ as the volume fraction of particles, D as their diffusion coefficient, h as the liquid height, and \dot{h} as its time derivative. Using the z -coordinate normal to the surface with an origin at the surface level, one obtains the differential equation⁴⁰

$$D \frac{\partial^2 \phi}{\partial z^2} + \dot{h} \frac{\partial \phi}{\partial z} - \frac{\partial \phi}{\partial t} = 0 \quad (1)$$

and the boundary condition at $z = 0$

$$\frac{\partial \phi}{\partial z} = -\frac{\dot{h}}{D} \phi \quad (2)$$

In the general case, the diffusion coefficient D writes as a Taylor series in ϕ in the dilute regime but tends to zero in the case of increasingly concentrated liquid as it approaches the sol–gel transition. Also, the evaporation rate \dot{h} decreases as the solvent rarefies near the surface, so that there is no analytical solution for eq 1. However, taking D and \dot{h} as constants (which seems reasonable at least at the beginning of the process), eqs 1 and 2 introduce a characteristic thickness, h^* , of the concentrated layer at the surface

$$h^* = \frac{D}{\dot{h}} \quad (3)$$

and also a characteristic time t^* needed for the liquid level to decrease by h^*

$$t^* = \frac{h^*}{\dot{h}} = \frac{D}{\dot{h}^2} \quad (4)$$

At short time ($t \ll t^*$) and near the surface ($z = 0$), eq 2 gives

$$\phi = \phi_h \exp(-z/h^*) \quad (5)$$

with

$$\phi_h = \phi_0 + \phi_0(t/t^*)^{1/2} \quad (6)$$

where ϕ_0 is the initial volume fraction of particles and ϕ_h the volume fraction at the surface. Note that the ratio $P_e = h/h^*$ is referred to as the Peclet number.³⁵ For $P_e \ll 1$, the liquid can be considered as homogeneous despite evaporation, and for $P_e \gg 1$, a more concentrated layer exists at the surface of the liquid. Values of these different characteristics are given in Table 1 for the three different systems here studied. Depending

Table 1. Characteristics of the Drying Conditions for the Three Colloidal Dispersions: a is the Particle Radius Determined by Small-Angle Neutron Scattering; D is the Diffusion Coefficient Derived from the Stokes–Einstein Relation $D = kT/6\pi\eta a$, with kT the Thermal Energy and η the Solvent Viscosity; h^* is the Characteristic Thickness of the Concentrated Surface Layer (Eq 3) and t^* is the Corresponding Characteristic Time (Eq 4); $P_e(0)$ is the Initial Peclet Number for the Initial Height $h(0) = 3.7$ mm of the Liquid^a

sample	a (nm)	D (10^{-11} m ² /s)	h^* (μ m)	t^* (s)	$P_e(0)$
SM30	4.7	4.6	767	12 778	5
HS40	7.9	2.7	450	7500	8
TMS0	12.8	1.7	283	4722	13

^aAll experiments were performed at room temperature $T \approx 23$ °C and a RH between 20 and 30%. Under these conditions, the average evaporation rate was evaluated from the liquid height z -scans to be around 6×10^{-8} m/s.

on the particle nature, the more concentrated surface layer can stay liquid or undergo a phase transition, leading to a solid gel layer, namely, a “skin”. Also, as evaporation continues, this skin may become very fragile and develop cracks, and the concentrated layer at this stage is referred to as a “crust”.

RESULTS AND DISCUSSION

Our studies address the structural properties at the air–liquid region of silica dispersions and their evolution during drying. Neutron reflectivity performed under specular conditions probe concentration gradients perpendicular to the liquid surface, but it will be clear in the following discussions that strong scattering from the particles in the surface region contributes to the principal signal from which we extract structure information.

Dispersion under Equilibrium Condition (No Evaporation). A dispersion of silica nanoparticles enclosed in the hermetic cell in the absence of evaporation remains in an equilibrium state. Development of a concentration gradient and accumulation of surface excess are not expected because of the charged and hydrophilic nature of the particles. Thus, for the silica dispersion under equilibrium, we expect a reflectivity curve that is characteristic of a homogeneous matrix with no vertical profile, which we refer to as a “Fresnel” curve.

Figure 2a shows reflectivity curves for HS40 (radius, $a = 7.9$ nm) at different bulk concentrations 2, 15, and 23% in volume.

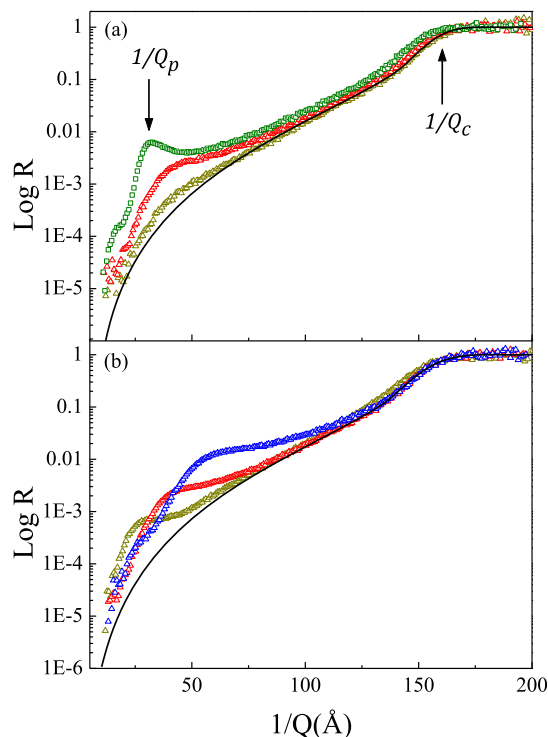


Figure 2. Reflectivity as a function of the inverse of the scattering vector $1/Q$ for dispersions under equilibrium (without evaporation): (a) HS40 ($a = 7.9$ nm) at different volume fractions: $\phi = 0.02$ (dark yellow), 0.15 (red), 0.23 (green); (b) at fixed volume fraction $\phi = 0.15$ for different particles sizes: SM30 ($a = 4.7$ nm, dark yellow), HS40 ($a = 7.9$ nm, red), TMS0 ($a = 12.8$ nm, blue). The solid lines are calculated Fresnel curves for $\phi = 0.02$ and 0.15 in (a,b), respectively. The wave vector value Q_c of the total reflection edge increases with particle concentration, and the structure peak position Q_p increases with particle concentration and decreases with particle size.

In this representation, reflectivity is plotted as a function of $1/Q$ for better display of the concentration-dependent total reflection edge, $Q_c = 4\sqrt{\pi\rho}$, where ρ is the scattering length density of the reflecting material. For silica dispersions, $\rho = \phi\rho_{\text{SiO}_2} + (1 - \phi)\rho_{\text{solvent}}$ where ϕ is the volume fraction of silica, $\rho_{\text{SiO}_2} = 3.64 \times 10^{-6} \text{ \AA}^{-2}$ is its scattering length density, and ρ_{solvent} is the scattering length density of the solvent. For a dispersion in H_2O , $\rho_{\text{solvent}} = \rho_{\text{H}_2\text{O}} = -0.56 \times 10^{-6} \text{ \AA}^{-2}$ and for $\phi \geq 0.3$, the Q_c of the dispersion lies within the Q -range of the experiment. For lower particle concentrations, however, Q_c is too low and a small amount of D_2O ($\rho_{\text{D}_2\text{O}} = 6.37 \times 10^{-6} \text{ \AA}^{-2}$) is added to increase ρ_{solvent} to render the Q_c accessible (the evolution of ρ_{solvent} during drying due to exchange of D_2O and H_2O from the air will be discussed in the next section). For initial dispersions, the values of Q_c measured under hermetic cover in the absence of evaporation are in good agreement with particle concentrations evaluated from gravimetry. The curves in Figure 2a show that Q_c increases with an increase in silica concentration as expected. Second, over a large Q -range, the reflectivity curves superimpose with the theoretical Fresnel curve (R_F) for a dispersion with a homogeneous vertical profile. In this figure, the solid line is calculated for a 2%

volume fraction silica dispersion but similar comparisons can be made for higher silica concentrations with their corresponding Fresnel curves. The third feature is less expected: the presence of a distinct peak whose intensity increases with concentration. The position Q_p of this peak is displaced toward higher- Q with increase in concentration, and at fixed volume fraction, toward lower- Q with increase in particle size (Figure 2b); in the latter case, total reflection occurs at approximately the same value of Q_c and the spectra show similar profiles with near-superposition with the Fresnel curve. For these experiments under equilibrium, the reflectivity curves remain unchanged, as monitored over a period of 24 h.

The concentration and size dependence of Q_p support its assignment to a structure peak due to scattering by the silica particles in the surface region, indicating the existence of a characteristic interparticle distance, $L_p = 2\pi/Q_p$. The dispersions show, accordingly, a decrease in L_p with particle concentration and an increase with particle size. This scattering signal in the reflectivity curve provides novel information on structural organization of the particles in the surface region of the liquid dispersion.

Dispersion during Evaporative Drying. In this section, we proceed to measure the structural evolution at the drying front of the dispersion during evaporation. The hermetic cell cover was removed to expose the dispersion to evaporation, and the structural evolution was tracked in situ by neutron reflectivity. Figure 3 shows the reflectivity spectra for HS40 as a function of drying time. These curves present features similar to those obtained under equilibrium condition: a large Fresnel-like region and a characteristic structure peak Q_p . In contrast, as drying proceeds, an increase in particle concentration is

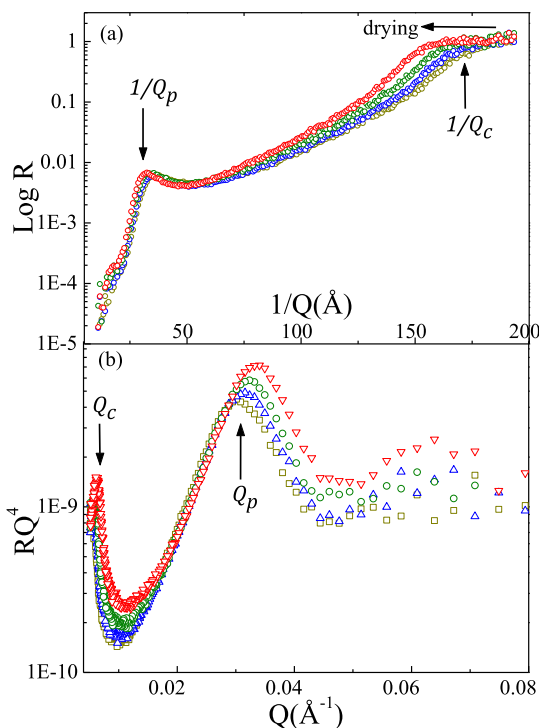


Figure 3. Evolution of reflectivity of HS40 at initial concentration $\phi_0 = 0.21$ during drying: 0 h (yellow), 3 h (blue), 5 h (green), 8 h (red). (a) R vs $1/Q$ highlights the shift in the critical reflection edge Q_c with increase in particle concentration; (b) RQ^4 vs Q highlights the structure peak around $Q_p \approx 0.3 \text{ \AA}^{-1}$ and its evolution during drying.

clearly evidenced by the increase in Q_c (increase in scattering length density) and a corresponding decrease in $1/Q_p = L_p/2\pi$ as the particles approach each other. This shift in the structure peak can be better visualized in a more classic plot of RQ^4 versus Q (Figure 3b). This representation enhances the high- Q region of the structure peak where a second-order oscillation is apparent at late-stage drying indicative of highly organized packing. Another noteworthy point in this plot is the higher intensity of the structure peak Q_p compared with Q_c of total reflection; this aspect, in the absence of Kiessig fringes (signature of reflectivity from interference of well-fined surface layers), lends strong support to the scattering rather than reflectivity origin of the structure peak.

Apart from the structure peak, the drying curves do not exhibit typical reflectivity profiles that are indicative of heterogeneous drying. Indeed, from Table 1, it appears that the expected thickness of the concentrated surface layer (a few hundred μm) is far beyond the value that can be observed with neutron reflectivity (a few hundred nm). Such a thick surface layer behaves, for the neutron beam, as the out-coming bulk medium. In this case, the total reflection edge Q_c is directly related to the scattering length density ρ_h in the surface region and thus to the volume fraction ϕ_h of particles at the surface described in eq 5. From $Q_c = 4\sqrt{\pi\rho_h}$ and $\rho_h = \phi_h\rho_{\text{SiO}_2} + (1 - \phi_h)\rho_{\text{solvent}}$, one obtains:

$$\phi_h = \frac{\frac{Q_c^2}{16\pi} - \rho_{\text{solvent}}}{\rho_{\text{SiO}_2} - \rho_{\text{solvent}}} \quad (7)$$

Note that the heterogeneous concentration profile of particles will be supported in the next section by a comparison of the surface concentration deduced from eq 7 and the total average particle concentration evaluated from the vertical z -scans of the liquid heights. Our measurements therefore do not inform on the thickness of the surface profile, rather, they allow us to follow the organization of the nanoparticles in the surface region and its evolution during drying, which are clearly quantifiable from the structure peaks. It will be seen in the next section that this structural information reveals the existence of the predicted crust layer as well as the onset of its formation.

Reporting drying of a dispersion as a function of time gives only a rough guide to the stage of the process. To reach a particular state, the drying time required depends on the initial concentration and other physical conditions, mainly temperature and RH. Here, the technique of neutron reflectivity and the configuration employed in our measurements present a unique approach to access directly the concentration of the surface layer from the total reflection edge Q_c . Therefore, irrespective of initial particle concentration and drying time and conditions, the particle concentration together with its corresponding structural organization can be extracted from the same reflectivity curve, and their evolution consolidated on a structure–concentration relation. This process is straightforward for $\phi \gtrsim 0.3$ (in pure H_2O) where Q_c falls within the measurement Q -range and the particle concentration can be deduced directly from eq 7. For lower particle concentrations, as mentioned before, a small volume fraction x of D_2O is added to the sample to increase the total scattering length density in order for the sample Q_c to be accessible experimentally. In this case, $\rho_h = \phi_h\rho_{\text{SiO}_2} + (1 - \phi_h)\rho_{\text{solvent}}$ with $\rho_{\text{solvent}} = x\rho_{\text{D}_2\text{O}} + (1 - x)\rho_{\text{H}_2\text{O}}$ where x is adjusted to obtain $\rho_{\text{solvent}} = 0.8 \times 10^{-6} \text{ \AA}^{-2}$ (after gravimetric

determination of the amount of H₂O in the initial sample). For drying experiments using this mixed solvent, to account for exchange of D₂O and H₂O due to exposure to water vapor in the air, an exchange curve is obtained by monitoring the change in ρ_{solvent} of an evaporating solvent containing the same volume fractions of H₂O and D₂O as in the initial silica dispersion. The effective value for ρ_{solvent} at each stage of drying is then used to evaluate ϕ (the z-scans for these measurements indicate similar evaporation rates for dilute dispersions and pure solvent).

The evolution of the structure peak during drying for TM50 ($a = 12.8$ nm) is shown in Figure 4. Starting at an initial

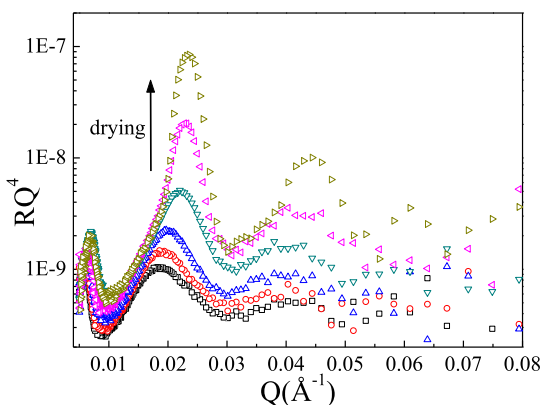


Figure 4. (a) RQ^4 vs Q for TM50 ($a = 12.8$ nm) showing the evolution of the structure peak during drying up to 12 h; initial particle volume fraction, $\phi_0 = 0.17$. The corresponding surface volume fractions, ϕ_h are 0.17 (black), 0.21 (red), 0.25 (blue), 0.32 (green), 0.35 (pink), and 0.39 (dark yellow).

volume fraction $\phi_0 = 0.17$, the sample is dried over a period of 12 h. At the end of this drying period, the volume fraction of particles at the surface is $\phi_h = 0.39$; to reach a similar state starting from $\phi_0 = 0.32$ requires less than 2 h, hence the relevance of relating structure to concentration instead of drying time. The large variation in concentration for TM50 allows us to track the evolution of the structure peak and its transition from a broad to a narrow well-defined peak with a distinct second-order oscillation for $\phi_h > 0.25$.

Figure 5 shows the interparticle distance $L_p = 2\pi/Q_p$ and the peak intensity as a function of ϕ_h at various drying stages for samples starting at different initial volume fractions ϕ_0 . So far, the values of Q_c have been assigned to a concentrated surface layer (with surface particle volume fraction ϕ_h) whose thickness exceeds the detection capability of the technique. To support this point, the inset in Figure 5a compares ϕ_h with the total average particle volume fraction $\bar{\phi}$ deduced from the vertical z-scans of the sample height performed at each stage of the reflectivity measurement. It can be seen that in all cases, $\phi_h > \bar{\phi}$ supporting a heterogeneous drying and the existence of a more concentrated layer at the surface. Note that within this concentrated layer, the concentration profile is almost flat. The initial thickness is predicted to be a few hundred microns (see Table 1), which is of the same order as the vertical depth probed and over which ϕ_h is averaged. Thus, irrespective of starting point and drying times, the results can be consolidated on the same structure–concentration curve. Interestingly, while the interparticle distance shows a monotonic decrease with particle concentration, the structure peak intensity (Figure 5b) shows an abrupt increase at $\phi_h > 0.35$, indicating

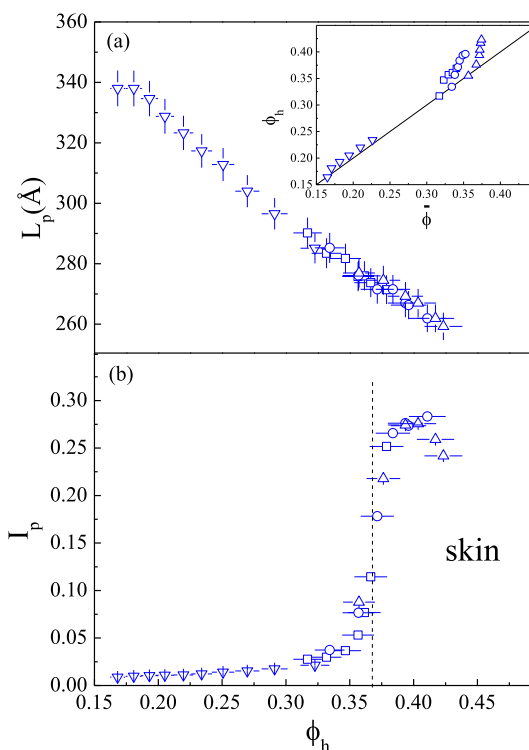


Figure 5. Structural evolution of TM50 during drying: (a) interparticle distance, L_p evaluated from the position of the structure peak Q_p vs ϕ_h deduced from eq 7; the inset shows that ϕ_h is always higher than the average concentration $\bar{\phi}$ derived from the z-scan of the sample height, supporting heterogeneous concentration profile (the solid line has a slope = 1); (b) relative intensity, I_p of the structure peak versus ϕ_h ; the inflection at $\phi_h \approx 0.37$ indicates a sol–gel transition, precursor to skin formation. Above $\phi_h \approx 0.42$, a skin is formed, detachable from the underlying liquid phase. The symbols indicate different series starting from different initial concentrations: $\phi_h = 0.17$ (inverted triangle), 0.32 (square), 0.33 (circle), and 0.36 (triangle).

an evolution to a highly organized state, as already noted previously from its transition from a broad to a sharp peak.

We assign the inflection at $\phi_h \approx 0.37$ to a transition from sol to wet-gel, precursor to skin formation. This threshold value is close to the values reported in previous studies (for $a = 8$ nm) on structures in bulk and in a confined geometry^{25,41} and in rheology studies that show a transition from Newtonian to shear thinning behavior of the dispersion.⁴² At this transition, the characteristic interparticle distance, $L_p \approx 270$ Å is still larger than the diameter of the particle. Beyond $\phi_h \approx 0.42$, the peak intensity decreases, a result attributed to onset of particle aggregation.^{25,30,41} The end-point in Figure 5 marks the appearance of stress-induced crimping at the edge of the sample in contact with the sample cell; this is followed rapidly by the appearance of small wrinkles in the middle of the sample surface and the experiments had to be stopped. At this stage, a macroscopic wet skin has formed, detachable from the bulk that is still liquid. We believe that this crucial stage initiates stress-induced surface fracture followed by bulk drying and simultaneous crack formation in the final dry sample.

Regarding the kinetics of formation of the surface layer, we mention briefly that the rate of formation of the surface layer depends on the balance of solvent evaporation and particle diffusion, as described in eqs 1–6. It is shown in eq 6 that the surface concentration ϕ_h varies linearly as \sqrt{t} for short times, t

$< t^*$ where t^* is a characteristic time defined in eq 4 and the values given in Table 1. Figure 6 shows a plot of eq 6: $(\phi_h/\phi_0) - 1$

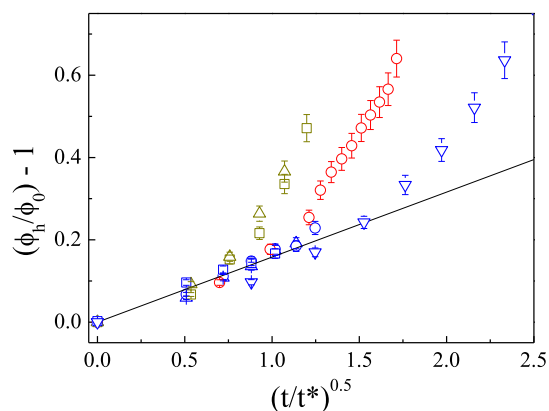


Figure 6. Surface concentration normalized by initial concentration versus normalized time (eq 6) using t^* values from Table 1: TM50 (blue) at different initial volume fractions, $\phi_0 = 0.17$ (inverted triangle), 0.32 (square), 0.33 (circle), and 0.36 (triangle); HS40 at $\phi_0 = 0.21$ (red); SM30 at $\phi_0 = 0.15$ (dark yellow, two separate series). The solid line is the best-fit through all points up to $t \approx t^*$. The divergence beyond $t \approx t^*$ is due to the very long drying times thereafter.

$- 1$ versus $\sqrt{(t/t^*)}$ for TM50 at different initial concentrations ($\phi_0 = 0.17, 0.32, 0.33,$ and 0.36), HS40 ($\phi_0 = 0.21$), and SM30 ($\phi_0 = 0.15$) using their respective t^* values from Table 1. These results show a relatively linear behavior up to $t \approx t^*$, beyond which they diverge due to the ensuing long drying times for samples starting at lower initial concentrations. The solid line is the best-fit curve through all of the samples up to $t \approx t^*$, with a slope $b = 0.16$; because $(1/b)^2 = t^*$, $b < 1$ suggests that the effective characteristic time, t_{eff}^* is

larger than t^* given in Table 1 calculated based on the Stokes–Einstein diffusion coefficient D . It appears therefore that an effective diffusion coefficient, $D_{\text{eff}} = t_{\text{eff}}^*/\bar{h}^2$ where $D_{\text{eff}} > D$ may be a more appropriate description for the system. Effective diffusion coefficients much higher than the Stokes–Einstein coefficient have indeed been measured and reported for similar silica dispersions.^{26,27}

Reversibility of Particle Organization. As mentioned before, two opposing mechanisms are at play during drying: evaporation concentrates the particles while diffusion promotes the return of particles from the surface to the bulk. Here, we test what happens when evaporation is stopped by putting back the hermetic cover above the dispersion at different drying stages. Figure 7 shows the evolution of the structure peak for TM50 with the time that has elapsed, Δt since putting back the hermetic cover. This evolution depends on the stage of drying—the concentration before the cover is put back— $\phi_h(\Delta t = 0)$. The reversibility of the peak intensity is rapid for $\phi_h(\Delta t = 0) = 0.36$: within 15 min, the intensity has decreased fourfold, indicating that the particles are still free to rearrange and that the concentrated surface layer is being diluted. This reversibility becomes increasingly slow with an increase in $\phi_h(\Delta t = 0)$, and at $\phi_h(\Delta t = 0) = 0.40$, the structure peak remains almost unchanged even up to $\Delta t > 1$ h. At this concentration juncture, particle mobility is almost completely blocked by interparticle cohesion, marking the threshold for skin formation. This stage also coincides with onset of significant particle clustering and aggregation, and a decrease in peak in intensity seen in Figure 5b. Note that up to $\phi_h = 0.39$, a sample that has undergone evaporation-stop cycles compares well with a sample that has been concentrated by continuous evaporation (without putting back the hermetic cover), suggesting that up to this concentration, particle organization is not history-dependent.

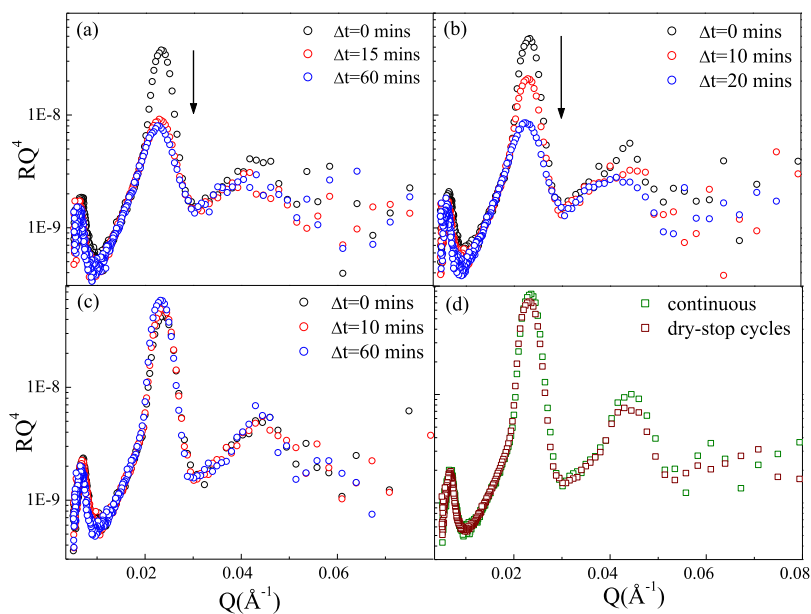


Figure 7. Reversibility of the structure peak at different drying stages for TM50. Evaporation is stopped by placing a hermetic cover above the dispersion. Δt indicates the elapsed time after placing the hermetic cover, for dispersions dried to different volume fractions: (a) $\phi_h(\Delta t = 0) = 0.36$, (b) $\phi_h(\Delta t = 0) = 0.38$, (c) $\phi_h(\Delta t = 0) = 0.40$; the arrow indicates the direction of increasing Δt ; (d) comparison of a sample that has undergone evaporation-stop cycles up to $\phi_h = 0.39$ and a sample concentrated by continuous evaporation to the same final concentration; the near-superposition of the curves suggests that up to this concentration, particle organization does not depend on sample history.

The neutron reflectivity experiments thus furnish information on the organization of particles in the surface region during evaporative drying, where construction of the surface layer is governed by a balance of evaporation and diffusion. They also reveal the concentration threshold for the transition from sol to wet-gel, precursor to skin formation. These information on the surface structure of a drying dispersion are important in the understanding of the initiation of surface stress and fracture. Next, we present complementary studies of the structural evolution in the bulk using SANS.

Structure in the Bulk Volume. Separate samples for SANS measurements are prepared by drying the dispersions in circular quartz cells in a horizontal position, and the sample cells sealed at different stages of drying. These measurements are therefore averaged over the entire thickness of the bulk sample (1 mm), and concentration gradient at the drying surface is considered negligible with respect to the macroscopic bulk volume. Furthermore, manipulation to close the sample cell and attaching it (from a horizontal drying position) to the sample holder in a vertical position contribute to some unavoidable remixing of surface and bulk.

The scattering curves, after subtraction of contribution from incoherent scattering, for TM50 dispersion at different stages of drying are presented in Figure 8. The curves display a

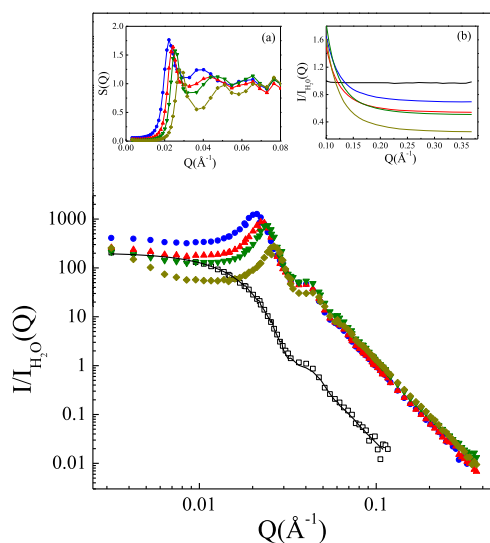


Figure 8. SANS curves of TM50 in dilute dispersion $\phi = 0.01$ in 10 mM NaCl (open symbol, the solid line is a fit to the form factor $a = 12.8$ nm, $\sigma/a = 0.14$), and in concentrated dispersion at initial volume fraction $\phi_0 = 0.31$ (close symbols) at different drying times: 0 h (blue), 1 h 30 (red), 3 h 45 (green), 14 h 45 (dark yellow). Inset (a): Corresponding structure factor $S(Q)$ extracted from the dilute dispersion form factor $P(Q)$; inset (b): corresponding H_2O incoherent scattering $\lim_{Q \rightarrow \infty} I/I_{\text{H}_2\text{O,inc}} = (1 - \phi)$.

structure peak that is displaced toward higher- Q as the concentration is increased with drying. A small oscillation to the right of the structure peak is also visible; it is characteristic of the particle size and is present also in the dilute dispersion. The coherent scattering intensity per unit volume for a dispersion of interacting spherical particles is the product of the form factor $P(Q)$ related to the size and shape of the individual particle and of the structure factor $S(Q)$ related to correlations of positions of particles⁴³

$$I(Q) = \phi \nu (\rho_{\text{SiO}_2} - \rho_{\text{solvent}})^2 P(Q) S(Q) \quad (8)$$

where ϕ is the volume fraction occupied by particles, ν the volume of each particle, and ρ_{SiO_2} and ρ_{solvent} the scattering length densities of silica and solvent, respectively. For a dilute suspension at 10 mM NaCl, the particles are noninteracting and $S(Q) = 1$ and the scattering curve reflects only the self-correlation of the particle $P(Q)$. For a spherical particle of radius a

$$P(Q) = \left[3 \frac{\sin(Qa) - Qa \cos(Qa)}{(Qa)^3} \right]^2 \quad (9)$$

This form is used to fit the dilute dispersion ($\phi \approx 0.01$) shown in Figure 8; the solid line is a fit with a radius $a = 12.8$ nm and a log-normal width $\sigma/a = 0.14$. For the interacting dispersions, to extract a form-independent effective structure factor, the scattering intensity is divided by the scattering curve of the dilute dispersion (with a multiplicative factor to impose $S(Q) \rightarrow 1$ at high- Q , see below for the discussion of this point). The resulting structure factor $S(Q)$ is shown in inset (a); from these curves, the interparticle distance, L_s is evaluated from the position Q_s of the correlation peak: $Q_s = 2\pi/L_s$.

To extract the volume fraction ϕ of particles from SANS measurements, several methods are possible. For a simple cubic lattice packing, the volume fraction is related to the position of the structure peak by $\phi = (a^3/6\pi^2)Q_s^3$. This expression works well for homogeneous systems such as that reported for very well dialyzed silica dispersions,²⁰ with different prefactor depending on the type of ordering. The volume fraction ϕ can also be obtained from data fitting using the mean spherical approximation model developed by Hayter and Penfold^{44–46} for repulsive hard spheres. This model requires knowledge of the particle charge and ionic strength, parameters that are not controlled in our samples and that evolve with drying. Furthermore, it is applicable only to homogeneous systems in the limit of moderate concentrations^{41,45,46} before the onset of particle attractions at higher concentrations. For our system, the reflectivity studies show that irreversible clustering sets in at $\phi \approx 0.4$ for TM50. This inhomogeneity in the system is also evidenced by the small-angle rise in the SANS curves. Therefore in our work, we extract ϕ using an approach specific to neutron scattering, by taking advantage of the incoherent scattering of protons in H_2O . The scattered intensity I per unit volume is the sum of coherent (I_{coh}) and incoherent (I_{inc}) contributions. For our two-component system, the total intensity can be written as $I = \phi I_{\text{SiO}_2,\text{coh}} + (1 - \phi) I_{\text{H}_2\text{O,inc}}$ since $I_{\text{SiO}_2,\text{inc}} = 0$ (no protons) and $I_{\text{H}_2\text{O,coh}} = 0$ (density fluctuations are negligible). Also, at high- Q , $\lim_{Q \rightarrow \infty} I_{\text{SiO}_2,\text{coh}} = 0$ leading to $\lim_{Q \rightarrow \infty} I = (1 - \phi) I_{\text{H}_2\text{O,inc}}$. Thus, dividing the scattering intensity per unit volume of the sample by the intensity of H_2O alone yields, at high- Q , a constant value equal to $1 - \phi$. Using this method, the volume fraction of particles is evaluated directly from the experimental curves, irrespective of the state of the particle dispersion. These values are shown in inset (b). This method, however, works only for a two-component system. For late-stage drying, the sample may be infiltrated by air leading to a decrease in the incoherent signal of H_2O and leading to an overestimation of ϕ . This effect can be seen in the last curve in inset (b) of Figure 8 for a late-stage drying sample at near-solid phase,

where the abrupt decrease in the incoherent level signals air penetration in the sample. For this last sample, an estimate range for ϕ may be derived from the scattered intensity measured at sufficiently high- Q so that $S(Q) \approx 1$. In this approach, we denote I as the scattered intensity measured for a dispersion at volume fraction ϕ of particles that display an effective contrast: $(\Delta\rho_{\text{med}})^2 = (\rho_{\text{SiO}_2} - \rho_{\text{med}})^2$ with their surrounding medium of scattering length density ρ_{med} . This medium is a continuous phase comprising water and air. In the absence of air (completely wet gel), $(\Delta\rho_{\text{med}})^2 = (\Delta\rho_{\text{H}_2\text{O}})^2 = 17.64$ and in the absence of water (completely dry gel), $(\Delta\rho_{\text{med}})^2 = (\Delta\rho_{\text{air}})^2 = 13.25$. From eq 8, we can write $(I/I_{\text{dil}})_{Q \rightarrow \infty} = (\phi/\phi_{\text{dil}}) \times ((\Delta\rho_{\text{med}})^2/(\Delta\rho_{\text{H}_2\text{O}})^2)$ where $\phi_{\text{dil}} = 0.01$ corresponds to the dilute dispersion of particles with contrast $(\Delta\rho_{\text{H}_2\text{O}})^2$. This leads to $(\phi/\phi_{\text{dil}}) = (I/I_{\text{dil}})_{Q \rightarrow \infty} \times ((\Delta\rho_{\text{H}_2\text{O}})^2/(\Delta\rho_{\text{med}})^2)$, and the two extreme conditions for $(\Delta\rho_{\text{med}})^2$ give the interval for (ϕ/ϕ_{dil}) that lies between $(I/I_{\text{dil}})_{Q \rightarrow \infty}$ and $(I/I_{\text{dil}})_{Q \rightarrow \infty} \times ((\Delta\rho_{\text{H}_2\text{O}})^2/(\Delta\rho_{\text{air}})^2)$. Using this method, the particle volume fraction of the last sample is estimated to fall in the range $0.48 < \phi < 0.63$, with high heterogeneity as revealed by the increase of the intensity at very small Q -values.

Comparison of Structures at the Interface and in the Bulk. During drying, particles at the surface concentrate and organize ahead of the bulk. To see if structural organization at the surface differs from that in the bulk, Figure 9a compares the evolution of the characteristic distance d in the concentrated surface layer ($d = L_p$ for reflectivity measure-

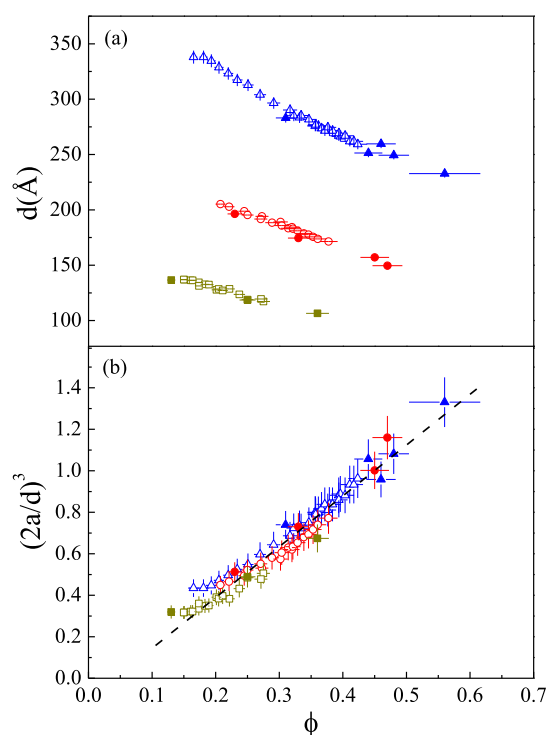


Figure 9. Evaporative consolidation of silica dispersions of difference particle sizes: $a = 4.7$ nm (dark yellow), 7.9 nm (red), 12.8 nm (blue). (a) Interparticle distance d vs volume fraction ϕ : in the surface layer (from neutron reflectivity, open symbols) and in the bulk (from SANS, closed symbols). (b) Corresponding size-normalized curves; collapse of the curves onto a near-master curve indicates similar structural evolution at the surface and in the bulk; the dotted line is a guide for the eyes.

ments) and in the bulk ($d = L_s$ for SANS measurements) as a function of the corresponding particle volume fraction ϕ ($\phi = \phi_h$ for reflectivity measurements). The structural organization shows a similar trend for the three samples, with no significant difference between the evolution at the surface and in the bulk. Figure 9b shows the same data normalized by particle size. The collapse of the three curves onto a master curve indicates that there is no marked difference in the structural organization for the range of particle sizes considered in this study. Also, the master curve is nearly linear, showing that in spite of the system inhomogeneity (revealed by the low- Q rise of the SANS intensity) the particle ordering varies with concentration as $\phi \propto (1/d)^3$; note that at high concentrations, $(2a/d)^3$ appears to exceed unity. Because two hard spheres cannot be closer than their diameter, we attribute this result to the effect of particle size polydispersity and to the log-normal distribution that has been used to fit the SANS data to determine a (a Zimm–Schulz distribution, e.g., would give smaller a -values).

We point out that the volume fractions of the final viscous paste, that just precedes solidification and fracture, decreases with particle size, as indicated by the last experimental points of the SANS results shown in Figure 9. These final wet-gel concentrations are $\phi = 0.56$, 0.47 , and 0.36 for particle size $a = 12.8$ nm (TM50), 7.9 nm (HS40), and 4.7 nm (SM30), respectively, and the dry gels that form thereafter are not expected to differ significantly in volume fractions. These gels therefore support a high water content trapped in the network of clusters that can render them more resistant to fracture. We find that to reduce fracture and to obtain large pieces of dry gels, slow drying over more than 1 month at high RH ($>50\%$) is necessary. Particle aggregation and resistance to fracture of the solid gel has also been reported elsewhere to be favored by slow drying.¹⁸ Note also that the maximum packing for SM30 is particularly low, closer to the value predicted for jamming or freeze-packing.⁴⁷ This may be related to a higher dissolution/precipitation rate of the small particle size of SM30 leading to network formation, and we may surmise that the sol–gel transition is also correspondingly lower; the dry gel in this case is visually transparent, while those for TM50 and HS40 are translucent. Both reflectivity and scattering results show that for these three samples, the degree of ordering decreases with the decrease in the particle size, as seen from the broader structure peaks shown in Figure S1.

Finally, for our samples that are used as received, the results show no detectable presence of colloidal crystals in the bulk phase such as those reported for very well dialyzed silica particles that nucleate at relatively low volume fractions, $\phi = 0.20$ – 0.25 ^{48,49} studied by small-angle X-ray scattering (SAXS); for similarly prepared dispersions in drying thin films studied by SAXS, no crystals were reported.²⁰ Other studies of dialyzed silica dispersions using SANS up to $\phi \approx 0.24$ ^{45,46} and $\phi \approx 0.4$ ⁵⁰ did not report the presence of crystalline structures either. For nondialyzed dispersions using SAXS, no colloidal crystals were reported.⁴¹ Interestingly, surface crystalline domains have been observed using atomic force microscopy for nondialyzed samples, but only under very high evaporation rates (RH $\approx 10\%$).¹⁸ It is argued that the very high evaporation rate prevents particle aggregation, leading to higher crystalline packing. Such a crystalline structure, however, comes at the expense of higher sample fragility compared with amorphous structures. It appears then that long-range ordering that produces crystal structures occurs

under specific dialysis protocols and under highly specific drying conditions. This interesting aspect of controlling amorphous–crystalline phases therefore has practical implications in obtaining materials for different functional and mechanical properties.

CONCLUSIONS

This work presents a study of the structural evolution of colloidal silica dispersions under evaporative drying for three Ludox samples, SM30, HS40, and TM50 with particle radii $a = 4.7, 7.9, \text{ and } 12.8 \text{ nm}$, respectively. Using neutron reflectivity, we focus on the air–dispersion interface, a region of initial stress development in macroscopic drying films and demonstrate heterogeneous evaporation for these systems. While the thickness of the surface layer is beyond the limit of measurement, the reflectivity curve shows a structure peak from the scattering of particles in the surface region that defines a characteristic correlation distance between particles. Under equilibrium conditions (without evaporation), this characteristic distance decreases with particle concentration and increases with the particle size. During evaporation, this particle correlation distance decreases as the dispersion is concentrated. Importantly, the corresponding particle concentration is extracted directly from the total reflection edge of the same reflectivity curve, enabling the time-dependent structural evolution to be converted to a structure–concentration relation. We show evidence that under evaporation, the structural properties measured by reflectivity pertain to those of a thick surface layer, more concentrated than that of the average bulk dispersion. These in situ drying experiments enable us to follow, in particular for TM50, the surface sol–gel transition, occurring at $\phi \approx 0.37$ and particle aggregation beyond $\phi \approx 0.40$ followed by formation of a macroscopic wet skin. Reversibility cycles, effected by placing a hermetic cover over the sample to stop the evaporation, further confirm irreversible particle cohesion in the surface layer that is precursor to this macroscopic wet-crust.

Complementary bulk measurements of dispersions at different stages of drying are carried out using SANS. Here, the particle concentration is evaluated directly from the high- Q incoherent signal from the H_2O in the sample. Comparison of the reflectivity and SANS results reveals similar structural evolution at the interface and in the bulk. Although the size-normalized curves collapse onto a master curve, suggesting similar organization behavior for the range of particle sizes considered, the degree of ordering, as indicated from the peak width, decreases with decrease in particle size. It is also observed that the SM30 gel ($a = 4.7 \text{ nm}$) supports a high water content—it forms, at late-stage drying, a viscous paste at relatively low concentration $\phi \approx 0.36$, suggesting jamming or freeze-packing.

ASSOCIATED CONTENT

Supporting Information

The Supporting Information is available free of charge on the ACS Publications website at DOI: [10.1021/acs.langmuir.8b03772](https://doi.org/10.1021/acs.langmuir.8b03772).

Comparison of the relative degree of ordering as indicated by the width of the structure peak in the surface layer from neutron reflectivity and in the bulk from SANS (PDF)

AUTHOR INFORMATION

Corresponding Author

*E-mail: Lay-Theng.Lee@cea.fr.

ORCID

Fabrice Cousin: 0000-0001-7523-5160

Lay-Theng Lee: 0000-0002-1421-8890

Author Contributions

The manuscript was written through contributions of all authors. All authors have given approval to the final version of the manuscript.

Notes

The authors declare no competing financial interest.

ACKNOWLEDGMENTS

This work was supported by the “Investissements d’Avenir” LabEx PALM (grant number: ANR-10-LABX-0039-PALM).

REFERENCES

- (1) Deegan, R. D.; Bakajin, O.; Dupont, T. F.; Huber, G.; Nagel, S. R.; Witten, T. A. Capillary Flow as The Cause of Ring Stains from Dried Liquid Drops. *Nature* **1997**, *389*, 827–829.
- (2) Keddie, J. Film Formation of Latex. *Mater. Sci. Eng., R* **1997**, *21*, 101–170.
- (3) Russel, W. B. Mechanics of Drying Colloidal Dispersions: Fluid/Solid Transitions, Skinning, Crystallization, Cracking, and Peeling. *AIChE J.* **2011**, *57*, 1378–1385.
- (4) Routh, A. F. Drying of Thin Colloidal Films. *Rep. Prog. Phys.* **2013**, *76*, 046603.
- (5) Baglioni, P.; Chelazzi, D.; Giorgi, R.; Poggi, G. Colloid and Materials Science for the Conservation of Cultural Heritage: Cleaning, Consolidation, and Deacidification. *Langmuir* **2013**, *29*, 5110–5122.
- (6) Giorgiutti-Dauphiné, F.; Pauchard, L. Painting Cracks: A Way to Investigate the Pictorial Matter. *J. Appl. Phys.* **2016**, *120*, 065107.
- (7) Léang, M.; Giorgiutti-Dauphiné, F.; Lee, L.-T.; Pauchard, L. Crack opening: from colloidal systems to paintings. *Soft Matter* **2017**, *13*, 5802–5808.
- (8) Atkinson, A.; Guppy, R. M. Mechanical Stability of Sol-Gel Films. *J. Mater. Sci.* **1991**, *26*, 3869–3873.
- (9) Hutchinson, J. W.; Suo, Z. Mixed Mode Cracking in Layered Materials. *Adv. Appl. Mech.* **1991**, *29*, 63–191.
- (10) Chiu, R. C.; Garino, T. J.; Cima, M. J. Drying of Granular Ceramic Films: I, Effect of Processing Variables on Cracking Behavior. *J. Am. Ceram. Soc.* **1993**, *76*, 2257–2264.
- (11) Pauchard, L.; Parisse, F.; Allain, C. Influence of Salt Content on Crack Patterns Formed through Colloidal Suspension Desiccation. *Phys. Rev. E: Stat., Nonlinear, Soft Matter Phys.* **1999**, *59*, 3737–3740.
- (12) Sibrant, A. L. R.; Pauchard, L. Effect of the Particle Interactions on the Structuration and Mechanical Strength of Particulate Materials. *Europhys. Lett.* **2017**, *116*, 49002.
- (13) Juillerat, F.; Bowen, P.; Hofmann, H. Formation and Drying of Colloidal Crystals Using Nanosized Silica Particles. *Langmuir* **2006**, *22*, 2249–2257.
- (14) Zhou, J.; Jiang, Y.; Doi, M. Cross Interaction Drives Stratification in Drying Film of Binary Colloidal Mixtures. *Phys. Rev. Lett.* **2017**, *118*, 108002.
- (15) Smith, M. I.; Sharp, J. S. Effects of Substrate Constraint on Crack Pattern Formation in Thin Films of Colloidal Polystyrene Particles. *Langmuir* **2011**, *27*, 8009–8017.
- (16) Perrin, L.; Pajor-Swierzy, A.; Magdassi, S.; Kamyshny, A.; Ortega, F.; Rubio, R. G. Evaporation of Nanosuspensions on Substrates with Different Hydrophobicity. *ACS Appl. Mater. Interfaces* **2018**, *10*, 3082–3093.
- (17) Caddock, B. D.; Hull, D. Lingua::EN::Titlecase. *J. Mater. Sci.* **2002**, *37*, 825–834.

- (18) Piroird, K.; Lazarus, V.; Gauthier, G.; Lesaine, A.; Bonamy, D.; Rountree, C. L. Role of Evaporation Rate on the Particle Organization and Crack Patterns Obtained by Drying a Colloidal Layer. *Europhys. Lett.* **2016**, *113*, 38002.
- (19) Parneix, C.; Vandoolaeghe, P.; Nikolayev, V. S.; Quéré, D.; Li, J.; Cabane, B. Dips and Rims in Dried Colloidal Films. *Phys. Rev. Lett.* **2010**, *105*, 266103.
- (20) Li, J.; Cabane, B.; Sztucki, M.; Gummel, J.; Goehring, L. Drying Dip-Coated Colloidal Films. *Langmuir* **2011**, *28*, 200–208.
- (21) Allain, C.; Limat, L. Regular Patterns of Cracks Formed by Directional Drying of a Colloidal Suspension. *Phys. Rev. Lett.* **1995**, *74*, 2981–2984.
- (22) Sarkar, A.; Tirumkudulu, M. S. Consolidation of Charged Colloids during Drying. *Langmuir* **2009**, *25*, 4945–4953.
- (23) Leng, J. Drying of a Colloidal Suspension in Confined Geometry. *Phys. Rev. E: Stat., Nonlinear, Soft Matter Phys.* **2010**, *82*, 021405.
- (24) Goehring, L.; Clegg, W. J.; Routh, A. F. Solidification and Ordering during Directional Drying of a Colloidal Dispersion. *Langmuir* **2010**, *26*, 9269–9275.
- (25) Boulogne, F.; Pauchard, L.; Giorgiutti-Dauphiné, F.; Botet, R.; Schweins, R.; Sztucki, M.; Li, J.; Cabane, B.; Goehring, L. Structural Anisotropy of Directionally Dried Colloids. *Europhys. Lett.* **2014**, *105*, 38005.
- (26) Ziane, N.; Salmon, J.-B. Solidification of a Charged Colloidal Dispersion Investigated Using Microfluidic Pervaporation. *Langmuir* **2015**, *31*, 7943–7952.
- (27) Loussert, C.; Bouchaudy, A.; Salmon, J.-B. Drying Dynamics of a Charged Colloidal Dispersion in a Confined Drop. *Phys. Rev. Fluids* **2016**, *1*, 084201.
- (28) Deegan, R. D. Pattern Formation in Drying Drops. *Phys. Rev. E: Stat., Nonlinear, Soft Matter Phys.* **2000**, *61*, 475–485.
- (29) Brutin, D.; Sobac, B.; Loquet, B.; Sampol, J. Pattern Formation in Drying Drops of Blood. *J. Fluid Mech.* **2011**, *667*, 85–95.
- (30) Bahadur, J.; Sen, D.; Mazumder, S.; Santoro, G.; Yu, S.; Roth, S. V.; Melnichenko, Y. B. Colloidal Nanoparticle Interaction Transition during Solvent Evaporation Investigated by in-Situ Small-Angle X-ray Scattering. *Langmuir* **2015**, *31*, 4612–4618.
- (31) Dufresne, E. R.; Corwin, E. I.; Greenblatt, N. A.; Ashmore, J.; Wang, D. Y.; Dinsmore, A. D.; Cheng, J. X.; Xie, X. S.; Hutchinson, J. W.; Weitz, D. A. Flow and Fracture in Drying Nanoparticle Suspensions. *Phys. Rev. Lett.* **2003**, *91*, 224501.
- (32) Dufresne, E. R.; Stark, D. J.; Greenblatt, N. A.; Cheng, J. X.; Hutchinson, J. W.; Mahadevan, L.; Weitz, D. A. Dynamics of Fracture in Drying Suspensions. *Langmuir* **2006**, *22*, 7144–7147.
- (33) Lee, W. P.; Routh, A. F. Why Do Drying Films Crack? *Langmuir* **2004**, *20*, 9885–9888.
- (34) Goehring, L.; Morris, S. W. Cracking Mud, Freezing Dirt, and Breaking Rocks. *Phys. Today* **2014**, *67*, 39–44.
- (35) Routh, A. F.; Zimmerman, W. B. Distribution of Particles during Solvent Evaporation from Films. *Chem. Eng. Sci.* **2004**, *59*, 2961–2968.
- (36) Style, R. W.; Peppin, S. S. L. Crust Formation in Drying Colloidal Suspensions. *Proc. R. Soc. A* **2011**, *467*, 174–193.
- (37) Tsapis, N.; Dufresne, E. R.; Sinha, S. S.; Riera, C. S.; Hutchinson, J. W.; Mahadevan, L.; Weitz, D. A. Onset of Buckling in Drying Droplets of Colloidal Suspensions. *Phys. Rev. Lett.* **2005**, *94*, 018302.
- (38) Pauchard, L.; Couder, Y. Invagination During the Collapse of an Inhomogeneous Spheroidal Shell. *Europhys. Lett.* **2007**, *66*, 667–673.
- (39) Boulogne, F.; Giorgiutti-Dauphiné, F.; Pauchard, L. The Buckling and Invagination Process During Consolidation of Colloidal Droplets. *Soft Matter* **2013**, *9*, 750–757.
- (40) Okuzono, T.; Ozawa, K.; Doi, M. Simple Model of Skin Formation Caused by Solvent Evaporation in Polymer Solutions. *Phys. Rev. Lett.* **2006**, *97*, 136103.
- (41) Kim, S.; Hyun, K.; Kim, Y. S.; Struth, B.; Clasen, C.; Ahn, K. H. Drying of a Charge-Stabilized Colloidal Suspension in Situ Monitored by Vertical Small-Angle X-ray Scattering. *Langmuir* **2013**, *29*, 10059–10065.
- (42) Di Giuseppe, E.; Davaille, A.; Mittelstaedt, E.; François, M. Rheological and Mechanical Properties of Silica Colloids: from Newtonian Liquid to Brittle Behaviour. *Rheol. Acta* **2012**, *51*, 451–465.
- (43) Windsor, C. G. An Introduction to Small-Angle Neutron Scattering. *J. Appl. Crystallogr.* **1988**, *21*, 582–588.
- (44) Hayter, J. B.; Penfold, J. An analytic structure factor for macroion solutions. *Mol. Phys.* **1981**, *42*, 109–118.
- (45) Penfold, J.; Ramsay, J. D. F. Studies of Electrical Double-layer Interactions in Concentrated Silica Sols by Small-angle Neutron Scattering. *J. Chem. Soc., Faraday Trans. 1* **1985**, 117–125.
- (46) Ramsay, J. D. F.; Scanlon, M. Structure and Interactions in Aqueous Colloidal Dispersions of Oxide Particles. *Colloids Surf.* **1986**, *18*, 207–221.
- (47) Torquato, S. Nearest-Neighbor Statistics for Packings of Hard Spheres and Disks. *Phys. Rev. E: Stat., Nonlinear, Soft Matter Phys.* **1995**, *51*, 3170–3182.
- (48) Chang, J.; Lesieur, P.; Delsanti, M.; Belloni, L.; Bonnet-Gonnet, C.; Cabane, B. Structural and Thermodynamic Properties of Charged Silica Dispersions. *J. Phys. Chem.* **1995**, *99*, 15993–16001.
- (49) Cabane, B.; Li, J.; Artzner, F.; Botet, R.; Labbez, C.; Bareigts, G.; Sztucki, M.; Goehring, L. Hiding in Plain View: Colloidal Self-Assembly from Polydisperse Populations. *Phys. Rev. Lett.* **2016**, *116*, 208001.
- (50) Robbes, A. S.; Cousin, F.; Méridet, G. Osmotic Stress on Concentrated Colloidal Suspensions: A Path Towards Equilibrium? *Braz. J. Phys.* **2009**, *39*, 156–162.